# Target Analysis of the Bacteriorhodopsin Photocycle Using a Spectrotemporal Model

**Ivo H. M. van Stokkum* and Richard H. Lozier**

*Department of Physics Applied Computer Science, Faculty of Sciences, Vrije Universiteit, Amsterdam, The Netherlands*

*Received: July 18, 2001; In Final Form: October 17, 2001*

The light-adapted bacteriorhodopsin (BR) photocycle was studied using time-resolved absorption spectroscopy, measuring at 15 wavelengths (380−700 nm), over five decades of time (1 $\mu$s to 0.3 s), over a temperature range of 5−35 °C, under four solvent conditions (pH 5, pH 7, pH 9, and pD 7), and under three polarization conditions (magic angle, parallel, and perpendicular). A spectrotemporal method was developed for simultaneous analysis of these data based upon species-associated spectra (SAS) and fraction cycling. Using mild spectral assumptions, the data were satisfactorily described by a fully reversible scheme with five spectrally different intermediates, and a reversible $M_1 \rightleftharpoons M_2$ spectrally silent transition, $K \rightleftharpoons L \rightleftharpoons M_1 \rightleftharpoons M_2 \rightleftharpoons N \rightleftharpoons O \rightarrow BR$. The estimated SAS were realistic. The free energy gradually decreased between the K and N or O intermediate by 10−20 kJ/mol. An alternative kinetic scheme containing an $M_1 \rightleftharpoons M_2$ transition that becomes unidirectional above pH 6 (Ludmann et al., *Biophys. J.* **1998**, *75*, 3110−3119) did not fit these data well. At all temperatures, the L to M transition was strongly retarded upon deuteration indicating strong involvement of proton translocation during this step. The polarization model analysis showed a reduced anisotropy of the $M_2$ intermediate, indicating retinal reorientation.

## Introduction

Bacteriorhodopsin (BR) functions as a light-driven proton pump.[1−10] The pumping cycle is initiated and energized by the absorption of a photon by the light-adapted state of BR. The BR photocycle was first studied by monitoring light-induced absorbance changes in the visible and modeled as an unbranched unidirectional cycle with five spectrally different intermediates[11]

$$BR \xrightarrow{h\nu} K \rightarrow L \rightarrow M \rightarrow N \rightarrow O \rightarrow BR$$

Later, it was realized that reversible reactions are involved, the simplest scheme being[12−15] $K \rightleftharpoons L \rightleftharpoons M \rightleftharpoons N \rightleftharpoons O \rightarrow BR$. However, even after 25 years, there still is much debate about necessary modifications of this simple scheme.

In BR, the number of rate constants needed to describe the all-trans photocycle, seven, is larger than the number of spectrally different intermediates.[16,17] This can be explained by spectrally silent transitions. The data from Xie et al.[17] were analyzed[15] using a model with six intermediates $K \rightleftharpoons L \rightleftharpoons X \rightleftharpoons M \rightleftharpoons N \rightleftharpoons O \rightarrow BR$, where the spectrum of X appears to be a mixture of L and M. Nagle[18] reanalyzed the Raman data from Ames and Mathies[12] arriving at the model $L \rightleftharpoons M_1 \rightarrow M_2 \rightleftharpoons N \rightarrow O \rightarrow BR$ (where $M_1 \rightarrow M_2$ represents a spectrally silent transition[19]) with an additional branching $L \rightarrow N$. Váró and Lanyi[20,21] used practically the same model, $K \rightleftharpoons L \rightleftharpoons M_1 \rightarrow M_2 \rightleftharpoons N \rightleftharpoons O \rightarrow BR$, but with an additional branching $N \rightarrow BR$. There are a number of differences in the data analyses of the above studies, which employ time-resolved difference absorption spectroscopy. It is important to distinguish the way that the spectral information is dealt with. On one hand, the spectra can be derived from certain (sometimes arbitrary) assumptions,[12,13,20,22−25] and the accompanying concentration profiles are subsequently analyzed with a kinetic model.[26,27] On the other hand, the difference absorption spectra can be free parameters to be estimated simultaneously with the kinetic, thermodynamic, and model parameters.[15,16,28] The latter approach is much more complicated[29] but less arbitrary because it is not necessary to choose the spectra of the intermediates in advance. The estimated difference absorption spectra also provide a test for the physicochemical relevance of the model used. For example, in ref 15, it was concluded that the model used was incomplete because the spectra of X and M appeared to be a mixture of L and M. A further drawback of that study was that two of the estimated activation energies (notably of the $O \rightarrow N$ back reaction at pH 5 and of the $X \rightarrow L$ back reaction at pH 7) were estimated to be negative, which is not realistic. The approach taken in ref 15, directly fitting a kinetic model to all data and judging it on the basis of the acceptability of the estimated physicochemical parameters, has been called target analysis.[30,31] Since that time, more sophisticated target analysis methods[31−35] have been developed, in which the model target consists of a kinetic scheme in combination with a model for the species associated (difference) spectra. These computationally intensive methods greatly benefit from the increased computer power. Therefore, it is timely to reanalyze high-quality data with state of the art modeling and parameter estimation methods.[36] Here, we analyze a five-dimensional superset of the data from Xie et al.[17] with a modification of the model used in ref 15 assuming a spectrally silent transition: $K \rightleftharpoons L \rightleftharpoons M_1 \rightleftharpoons M_2 \rightleftharpoons N \rightleftharpoons O \rightarrow BR$. Note that, contrary to refs 20 and 26, in our model the spectrally silent transition from $M_1 \rightleftharpoons M_2$ is not irreversible above pH 6 and that the model is unbranched. Furthermore, we introduce a new type of target analysis, in which we add spectral assumptions to a kinetic model with thermodynamic parameters for the microscopic rates.[15,29] The crucial spectral assumption is that the M state(s) does not absorb above 540 nm. The combination of a model for the time domain (the kinetic scheme) and for the spectral domain (see Materials and Methods) is called a spectrotemporal model. It can naturally

* To whom correspondence should be addressed. Department of Physics Applied Computer Science, Division of Physics and Astronomy, Faculty of Sciences, Vrije Universiteit, De Boelelaan 1081, 1081 HV Amsterdam, The Netherlands. Tel: 31 20 4447868. Fax: 31 20 4447899. E-mail: ivo@nat.vu.nl.

10.1021/jp0127723 CCC: $22.00 
Published on Web 03/13/2002

be extended to describe polarized data. The quality of the target analysis can be judged from the meaningfulness of the estimated parameters (spectra, rate constants, free-energy time profiles, and anisotropy changes; see Materials and Methods).

The isotope effect in the BR photocycle has been studied at a single temperature.[37,38] Here, we perform a target analysis of both $H_2O$ and $D_2O$ data as a function of temperature. The estimated equilibria are translated to the evolution of thermodynamic variables during the photocycle. The changes in polarized absorption during the BR photocycle have remained elusive for decades already. A mandatory prerequisite for any analysis of polarized data is a magic angle model, which includes the bleach spectrum. Through the use of our target analysis scheme, it is investigated whether a model with an initial anisotropy characteristic for each intermediate and a temperature-dependent anisotropy decay rate reflecting membrane tumbling can describe the parallelly and perpendicularly polarized data.

## Materials and Methods

The data from Xie et al.[17] involve seven temperatures (from 5 to 35 °C in steps of 5 °C), three pH values (5, 7, and 9), and 15 wavelengths (between 380 and 700 nm). At 5, 15, 25, and 35 °C, measuring wavelengths were 420, 540, 600, and 660 nm, whereas at 10, 20, and 30 °C, eleven additional wavelengths were measured (380, 400, 440, 460, 520, 560, 580, 620, 640, 680, 700 nm). Traces were measured at 47 (logarithmically equidistant) time points between 1 $\mu$s and about 0.3 s. Sample preparation and experimental methods have been described in detail before.[17,39] These magic angle data are complemented by two other data sets: (a) measurements in $D_2O$ at pD 7 at five temperatures (from 10 to 30 °C in steps of 5 °C) and (b) $\Delta A_{\parallel}$ and $\Delta A_{\perp}$ measurements (note that the total amount of data is 4 times larger than that in refs 15 and 17). The sample preparation for the deuterated sample at pD 7 was the same as that for pH 7 except that $D_2O$ was used as the solvent. The light-induced absorption changes, $\Delta A_{\parallel}$ and $\Delta A_{\perp}$, were measured with the polarization of the measuring beam parallel and perpendicular to the polarization of the actinic laser beam, respectively. These data were collected during the same experiments on the same samples and using the same flash system as those for the magic angle data collection. With the use of computer control, the polarization of a linear polarizer for the measuring beam was sequentially set to be at zero (parallel), 54.3° (magic angle), and 90° (perpendicular) with respect to the polarization of the actinic laser. At each polarization, the data were averaged over 10 flashes, before moving to the next polarization. A total of 100 flashes were averaged for each polarization.

**Target Analysis Model Formulation.** According to the Beer−Lambert law, the spectroscopic properties of a mixture of components are a superposition of the spectroscopic properties of the components weighted by their concentration. Thus the perfect, noise-free, time-resolved difference absorption, $\Delta A$, is a superposition of the contributions of the $n_{\mathrm{comp}}$ different components:

$$\Delta A(t,\lambda) = \sum_{l=1}^{n_{\mathrm{comp}}} c_l(t)\Delta\epsilon_l(\lambda) \qquad (1)$$

where $c_l(t)$ and $\Delta\epsilon_l(\lambda)$ denote, respectively, the concentration and species-associated difference spectrum (SADS) of component $l$. By definition, $\Delta\epsilon_l(\lambda) = \epsilon_l(\lambda) - \epsilon_0(\lambda)$, where $\epsilon_l(\lambda)$ is the species-associated spectrum (SAS) of component $l$ and $\epsilon_0(\lambda)$ is the ground-state bleach spectrum. Regarding eq 1, we note that the quantity that will be estimated is the product $c_l\Delta\epsilon_l$, which in itself is insufficient for the determination of the absolute values of $c_l$ and $\Delta\epsilon_l$. Because in the photocycle no molecules are lost, the relative concentrations of the components can be estimated and thus also the relative amplitudes of their difference spectra. Here, we take $c_1(0) \equiv 1$, and thus, all concentrations are relative to the concentration right after excitation of the first photocycle state in our model, K.

In matrix notation, eq 1 reads

$$\Delta A = \mathbf{C}(\mathbf{E} - \epsilon_0)^{\mathrm{T}} = \mathbf{C}\mathbf{E}^{\mathrm{T}} - \mathbf{C}1\epsilon_0{}^{\mathrm{T}} \qquad (2)$$

where the $m \times n$ matrix, $\Delta A$, denotes the measured time-resolved difference absorption traces, measured at $m$ time instants $t_i$, and $n$ wavelengths $\lambda_j$. The matrixes $C$ and $E$, of dimension $m \times n_{\mathrm{comp}}$ and $n \times n_{\mathrm{comp}}$, respectively, contain in column $l$ the concentration profile and SAS of component $l$. The matrix-vector product $\mathbf{C}1$ is a vector containing the sum of the concentrations of the photocycling intermediates, which is equal to the ground-state depletion. By use of the vector representation of a matrix and the Kronecker product ($\otimes$),[40] eq 2 can be rewritten

$$\mathrm{vec}(\Delta A) = (I_n \otimes \mathbf{C})\mathrm{vec}(\mathbf{E}^{\mathrm{T}}) - (\tilde{\epsilon}_0 \otimes \mathbf{C}1)\mathrm{fc} \qquad (3)$$

where we have substituted for the bleach spectrum $\epsilon_0 = \mathrm{fc}\cdot\tilde{\epsilon}_0$, with fc, the fraction cycling, and $\tilde{\epsilon}_0$, the (measured) ground-state spectrum of the sample before excitation. When we use a kinetic model, $\mathbf{C}(\theta)$, we can express eq 3 as a separable nonlinear model:[29,40,41]

$$\mathrm{vec}(\Delta A) = [I_n \otimes \mathbf{C}(\theta) - \tilde{\epsilon}_0 \otimes \mathbf{C}(\theta)1]\begin{bmatrix}\mathrm{vec}(\mathbf{E}^{\mathrm{T}})\\ \mathrm{fc}\end{bmatrix} \qquad (4)$$

with conditionally linear parameters $\mathrm{vec}(\mathbf{E}^{\mathrm{T}})$, the SAS, and fc. This least-squares problem is unsolvable because the last column $-\tilde{\epsilon}_0 \otimes \mathbf{C}(\theta)1$ is a linear combination of all of the other columns. Therefore, an extra assumption is necessary to remove this dependence. An obvious assumption is that the M state(s) does not absorb above 540 nm, thus removing these elements from $\mathrm{vec}(\mathbf{E}^{\mathrm{T}})$ and deleting the accompanying columns in $I_n \otimes \mathbf{C}(\theta)$.

An advantage of the fc target analysis is that the SAS that are estimated now should represent the "true" spectra of the intermediates and thus provide for a direct check of the plausibility of the model. A prerequisite for the fc target analysis is the availability of a high-quality ground-state absorbance spectrum.

The generalization of eq 4 to a simultaneous target analysis of multiple experiments is straightforward. For each extra experiment, an overall scaling parameter is needed to account for variations in the product of sample OD, fraction cycling, and intensity of the actinic flash.

A note on the computational complexity is in order here. With the full data set, the dimensions of the matrix in eq 4 are 32 702 rows (data points) and 57−63 columns (conditionally linear parameters). Operations with this large matrix dominate the computation time. On an IBM RS6000/270 workstation (with 4 MB L2 cache, running at 375 MHz), an iteration takes about 20 s. Thus, a minimization typically requires 10 min.

**Inclusion of Parallel and Perpendicular Data.** To include the parallel and perpendicular data, we extend the model for the magic angle data from eq 2 by multiplying the concentration of each component $i$ (BR or the intermediates K, L, $M_1$, $M_2$, N,

and O) by $1 + 2r_i(t)$ for parallel data and by $1 - r_i(t)$ for perpendicular data. The full model then reads

$$\begin{bmatrix}\Delta A(t,\lambda)\\ \Delta A_{\parallel}(t,\lambda)\\ \Delta A_{\perp}(t,\lambda)\end{bmatrix} = \sum_{l=1}^{n_{comp}} c_l(t)\epsilon_l(\lambda)\begin{bmatrix}1\\ 1+2r_l(t)\\ 1-r_l(t)\end{bmatrix} - \mathrm{fc}\cdot\tilde{\epsilon}_0 \begin{bmatrix}1\\ 1+2r_{BR}(t)\\ 1-r_{BR}(t)\end{bmatrix}\sum_{l=1}^{n_{comp}} c_l(t) \quad (5)$$

For the time dependence of the anisotropy an exponential decay model was used:

$$r_i(t) = r_{0i}\exp(-k_{tumb}t) \quad (6)$$

in which $k_{tumb}$ is the rate of membrane tumbling and $r_{0i}$ is the anisotropy at time zero of component *i*. To minimize the number of anisotropy parameters, we assume that $k_{tumb}$ depends on temperature only, $r_{0,BR}$ can depend on pH, whereas $r_{0i}$ can be different for $H_2O$ and $D_2O$. Thus for all data, we needed seven $k_{tumb}$ parameters, four $r_{0,BR}$ parameters, and $2 \times 6 = 12$ $r_{0i}$ parameters for the photocycle intermediates in $H_2O$ and $D_2O$. The $r_{0i}$ were constrained to be not larger than $r_{0,BR}$.

**Estimation of the Rate Constants.** *Thermodynamic Parameters.* To estimate the 11 rate constants in the model K ⇌ L ⇌ $M_1$ ⇌ $M_2$ ⇌ N ⇌ O → BR, a number of assumptions are necessary.[15,29] The temperature dependence of the rate constants is described by an Eyring relationship:[42]

$$\ln(K^{\#}) = \frac{\Delta S^{\#}}{R} - \frac{\Delta H^{\#}}{RT} \quad (7)$$

where $K^{\#} = (kh)/(k_BT)$ is the activation equilibrium constant and $\Delta S^{\#}$ and $\Delta H^{\#}$ are the entropy and enthalpy changes of activation. Because of the limited temperature range of 5−35 °C, the correlation between the estimates of the $\Delta S^{\#}$ and $\Delta H^{\#}$ parameters describing a certain rate was found to be 0.999. Therefore, instead of $\Delta S^{\#}$, the rate at 20 °C, $k_{20}$, could be estimated as well. This parameter was found to be uncorrelated with the $\Delta H^{\#}$ parameter. The parameters $\Delta H^{\#}$ (and also $k_{20}$) were constrained to be nonnegative. For each solvent condition, 22 parameters are needed to describe the temperature dependence of the 11 rate constants.

*Spectral Parameters.* To reduce the number of free parameters, the spectral parameters, the SAS, were linked for the data measured at different temperatures and different pH. Negligible temperature dependence of the M spectrum was shown[43] in the range 5−25 °C, whereas negligible pH dependence of the intermediate spectra was found[22] in the range pH 4.5−9. Next to the above-mentioned assumption, that the M state(s) does not absorb above 540 nm, several other assumptions were found to be useful to reduce the number of free parameters. The N and O intermediates were assumed not to contribute to the difference absorption below 460 nm. The L and N intermediates were assumed not to absorb at 680 and 700 nm. Models with or without these two assumptions were tested. The SAS for $M_1$ and $M_2$ were independently estimated and turned out to be almost identical.

*Scaling Parameters.* Ideally, the parameters of the spectrotemporal model would be limited to meaningful parameters: $k_{20}$, $\Delta H^{\#}$, SAS, fc, and anisotropy (vide supra). Unfortunately, in addition to the fraction cycling parameter for the first experiment (20 °C, pH 7), for each extra experimental condition (pH, pD, or temperature) an overall scaling parameter is needed to account for variations in the product of sample OD and intensity of the actinic flash. With 26 experiments, this adds up to $1 + 25 = 26$ parameters.

A scaling parameter was introduced in ref 15 for each trace to correct for variations in the intensity of the actinic flash. This parameter was fixed at 1 for the first experiment. Thus in ref 15, the $H_2O$ magic angle data were globally fitted using six spectra (of 15 parameters each), $11 \times 2 \times 3 = 66$ thermodynamic parameters, and 168 scaling parameters.

Here, we analyze 4 times more data (because we include $D_2O$, parallel, and perpendicular data). We add 22 thermodynamic parameters (for the $D_2O$ experiments) and 23 anisotropy parameters (vide supra) but need only 26 parameters for fraction cycling and scaling. Furthermore, depending upon the spectral assumptions, the number of spectral parameters can decrease from 90 to 56. The minimal number of parameters for the fc target analysis of the 76 different experiments (comprising 32 702 data points) is 193. After convergence of the fit a refinement can be applied. Systematic trends in the residuals due to variations in the intensity of the actinic flash can be removed by estimating a scaling parameter for each trace. A common scaling parameter was estimated for the three polarization conditions. Generally, these 235 scaling parameters were found to vary randomly, 94% of them were between 0.9 and 1.1. These scaling parameters were kept fixed in a subsequent refined fit.

*Weighting and Convergence.* First, we performed an unweighted nonlinear least-squares fit. A very small number of outliers were detected, which were given a negligible weight in a subsequent weighted fit.[44] Furthermore, data at different wavelengths were weighted so that the weighted rms error was approximately wavelength-independent. From 620 to 700 nm, the weight increased from 1.4 to 7, whereas from 380 to 460 nm, the weight varied between 1.4 and 2. The weight was equal to 1 for the magic angle data between 520 and 600 nm. The parallel and perpendicular data were also weighted so that the weighted rms error was approximately polarization-independent.

To safeguard against local minima,[29,36] after convergence, each parameter was disturbed by an amount proportional to several times the estimated standard error, and the fit was restarted from these initial values. In this way, the parameter space was checked locally for a possible smaller minimum. Furthermore, the correctness of the method and the program was verified by fitting simulated data with a very high signal-to-noise ratio ($10^8$). When distant starting values of the parameters were used, convergence to the true parameter values was achieved.

## Results

Part of the magic angle data is shown as dots in Figure 1. At 660 nm (top row), the first decay phase is due to the decay of the red-shifted intermediate K, whereas the maximum in the millisecond time range is attributed to the red-shifted intermediate O. The amplitude of this maximum increases with temperature; at pH 9, the O intermediate becomes clearly visible at the highest temperatures (yellow, cyan, and magenta). At 600 nm (second row), the first decay phase corresponds to the K to L transition, whereas the second phase corresponds to the L to M transition. At pH 9, the recovery of the BR bleach (540 and 600 nm) clearly differs from pH 5 and pH 7 because of the abundance of intermediate N. At 420 nm (fourth row), the signal is mainly caused by the blue-shifted intermediate M, which at pH 9 is present at early times. With pD 7, the L to M transition is slowed down by 1 order of magnitude (compare first column of Figure 2 and second column of Figure 1). All these qualitative

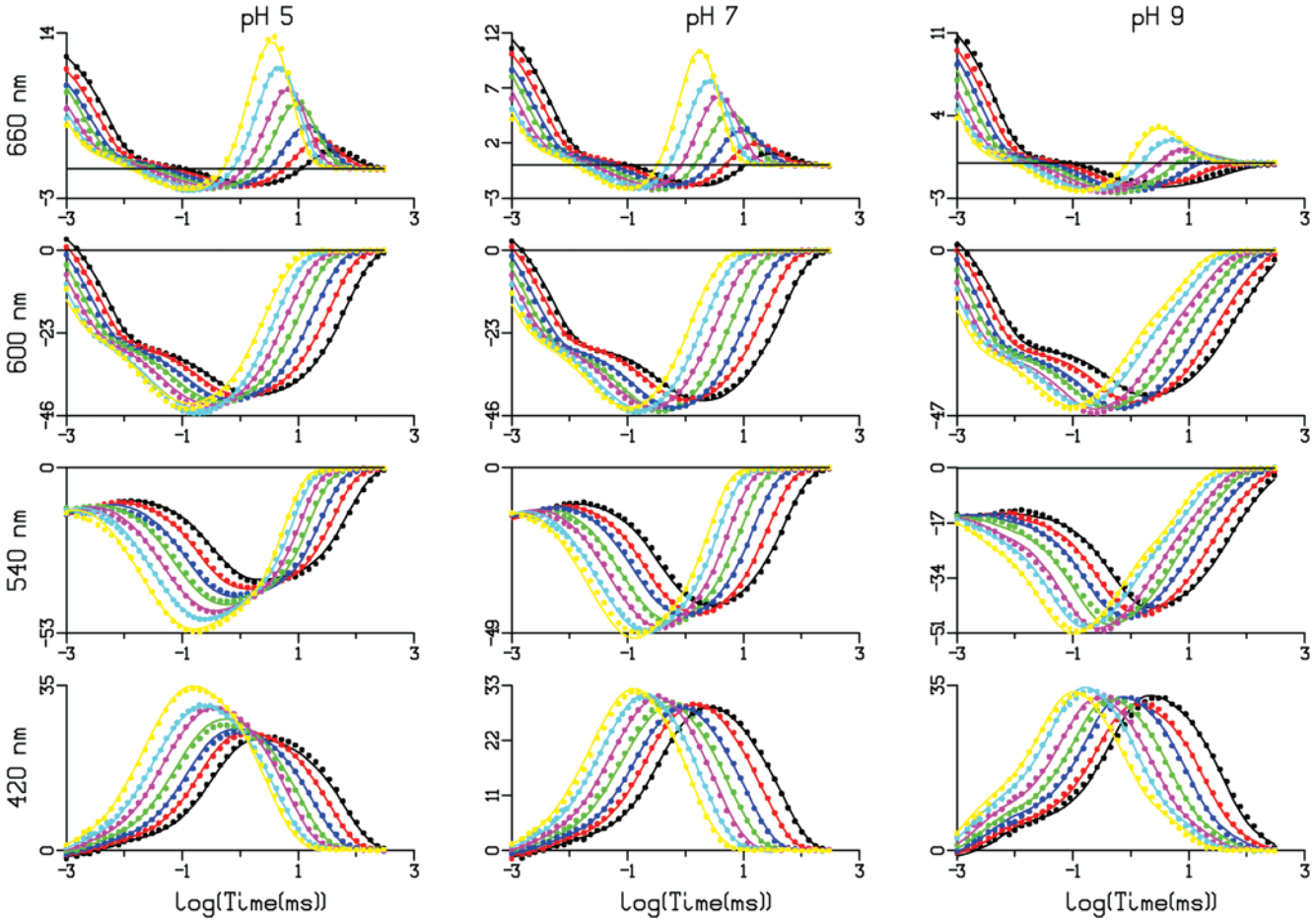


**Figure 1.** Comparison of the (scaled) experimental magic angle data of the BR photocycle (dots) and fit curves obtained by target analysis using the spectrotemporal model with the kinetic scheme K ⇌ L ⇌ $M_1$ ⇌ $M_2$ ⇌ N ⇌ O → BR. From left to right, data are presented for pH 5, 7, and 9. At the left, each wavelength (420, 540, 600, or 660 nm) is written. The traces are shown at seven temperatures (5−35 °C in 5 °C steps from right to left; corresponding colors are black, red, blue, green, magenta, cyan, and yellow). Note the differences in vertical scale.

observations can only be quantitated with the help of a detailed kinetic model. The $H_2O$ magic angle data were globally fitted using the model K ⇌ L ⇌ $M_1$ ⇌ $M_2$ ⇌ N ⇌ O → BR. For comparison, the unweighted rms error of the fit of the $H_2O$ magic angle data (0.4 mOD) was the same as in ref 15. As explained in the methods, for the fit presented here, the data were weighted so that the weighted rms error (0.755 mOD) was approximately wavelength-independent. The residuals of the weighted fit are shown in Figure 3; small trends are visible in the residuals of some of the traces, but no obvious pattern is present. We will return to possible causes of these correlated residuals in the discussion. At 420 nm in Figure 2, the L contribution to the fit results in negative residuals (see, Figure S.1 of Supporting Information), which seems to be erroneous. Forcing the L difference absorption to be zero below 430 nm resolves the problem at 420 nm, but causes larger residuals in other places, arriving at a weighted rms error of 0.790 mOD. The assumptions of temperature and pH/pD independence of the spectra most probably are an oversimplification causing systematic deviations. When the data and fits in Figures 1 and 2 are compared, overall the agreement is considered good. The concentration profiles (Figure 4) show that the O population (black) rises to 30% of the fraction cycling at high temperature and pH 5. At pH 9, the N population (green) rises to 54% of the fc at all temperatures. Some L fraction (red) remains present at the lowest temperatures until 100 ms. The population of $M_1$ + $M_2$ (blue) dominates the middle part of the photocycle at pH 5 or 7, with $M_1$ (dashed blue lines) remaining present. In contrast, at pH 9, $M_1$ appears early but disappears readily. This early appearance of M at pH 9 is well-known.[45−48]

The estimated fraction cycling parameter was 0.19 at pH 7 and 20 °C. All estimated SAS (Figure 5A) showed a single band, in contrast to Figure 3 in ref 15 in which the spectra of X and M both exhibited two absorption bands. The SAS appear to agree well with those estimated from time-gated spectra,[22] although small differences are apparent in the relative magnitudes of L and N. We will return to these differences in the discussion. Borucki et al.[49] estimated similar K and L spectra, also around 420 nm. Note that the standard errors in the O SAS (black) are relatively large. The $M_1$ SAS (dashed blue lines) is estimated to be somewhat smaller than the $M_2$ SAS, in particular at 420 nm.

The estimated thermodynamic parameters, $k_{20}$ and $\Delta H^{\#}$, are collated in Table 1. Large differences in $k_{20}$ are present between pH 7 and pD 7, in particular for the L ⇌ $M_1$ transition and the O → BR transition, confirming the single-temperature studies.[37,38] The $k_{20}$ of N → O drops at pH 9, whereas $k_{20}$ of the O → BR transition drops at pH 5, both in accordance with ref 46. The parameters for the $M_1$ ⇌ $M_2$ transition cannot be estimated precisely, except for pH 9. At pH 9, the L ↔ $M_1$ equilibrium is associated with huge, uncertain $k_{20}$, which was also reported in ref 26. Because at pH 9 the O state is only populated for the highest temperatures (Figure 1, Figure 4), the uncertainties in

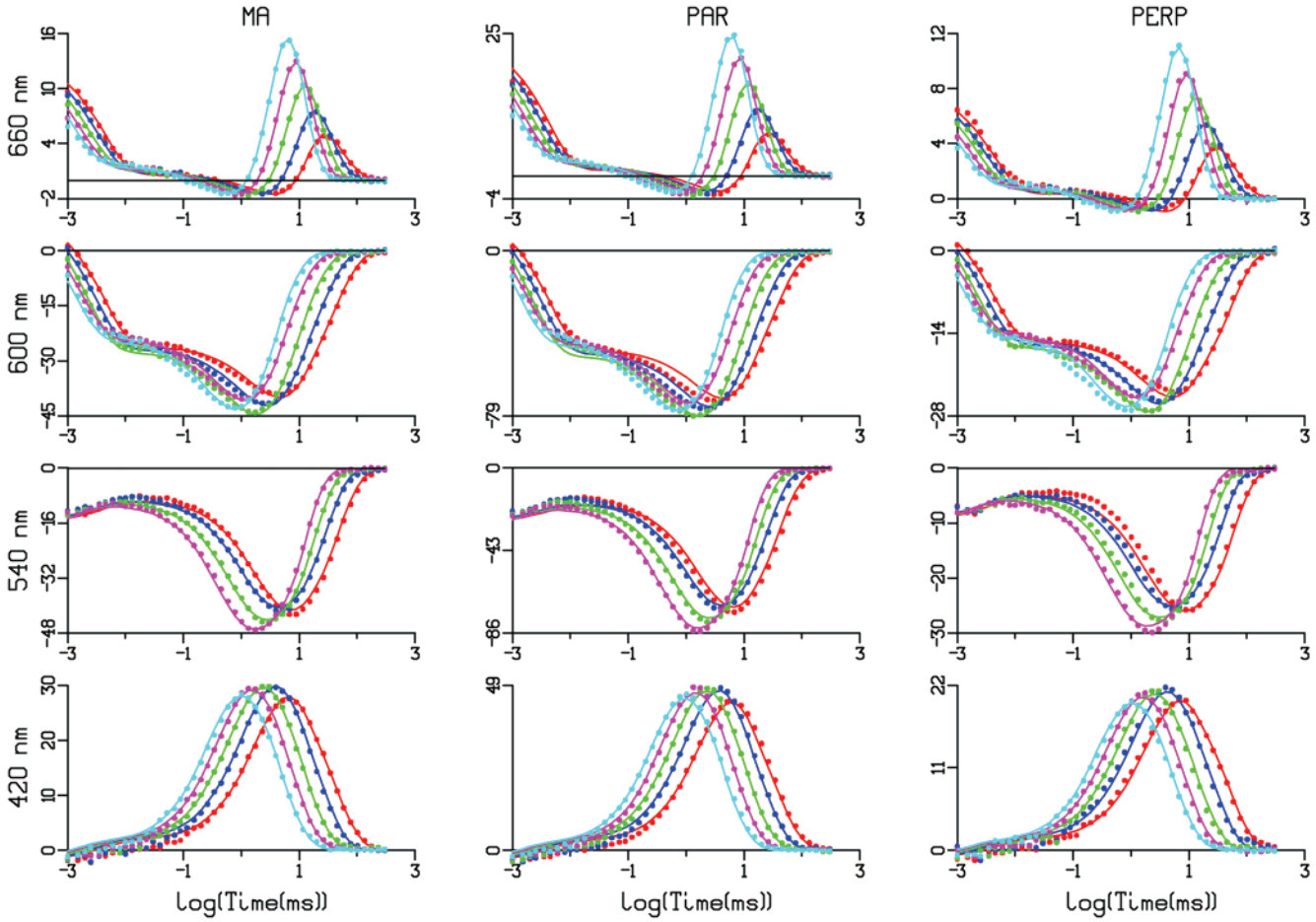


**Figure 2.** Comparison of the (scaled) pD 7 experimental data of the BR photocycle (dots) and fit curves obtained using the spectrotemporal model. From left to right, data are presented for magic angle, parallel, and perpendicular polarization. At the left, each wavelength (420, 540, 600, or 660 nm) is written. The traces are shown at five temperatures (10−30 °C in 5 °C steps from right to left; corresponding colors are red, blue, green, magenta, and cyan). Note the differences in vertical scale.

the $k_{20}$ and $\Delta H^{\#}$ parameters of the O → BR and O → N transition become relatively large.

The entropy, enthalpy, and free energy changes during the photocycle are depicted in Figure 6. The K ⇌ L transition is almost identical for the four solvent conditions, apart from the small isotope effect (Table 1). The $\Delta G$ barrier of the L ⇌ $M_1$ transition coincides for pH 5 (black) and pH 7 (red). With pH 9 (blue), this barrier is 5−10 kJ/mol lower, whereas with pD 7 (green), it is 5−8 kJ/mol higher. With pH 9, however, the $M_1$ $\Delta G$ level is higher than that of L, resulting in a fast establishment of the equilibrium, which is dominated by L. This early M is clearly visible at 420 nm in Figure 1 (fourth row, third column). Also, the $\Delta S$ and $\Delta H$ curves start to deviate with the L ⇌ $M_1$ transition for these solvent conditions. The vertical error bars in $\Delta S$ and $\Delta H$ increase toward the end of the photocycle. Apparently, the temperature range is too small to precisely separate $\Delta S^{\#}$ and $\Delta H^{\#}$ effects. Note that the error bars in $\Delta G$ are relatively smaller, because of the covariance of the $\Delta S^{\#}$ and $\Delta H^{\#}$ parameters.

The free-energy gap between $M_1$ and $M_2$ is always smaller than 10 kJ/mol. The energy difference between the K and N or O state is 10−20 kJ/mol (Figure 6, top), which compares well with the literature value[10] of 15−25 kJ/mol. The gradual decrease of free energy was also found when testing different spectral assumptions. The energy content of the K intermediate was estimated[51,52] to be 40 ± 10 kJ/mol. At 35 °C, the transition from K to O is estimated to cost less than 20 kJ/mol, which leaves about 20 kJ/mol for the O to BR transition. The large free-energy loss in the last step of the photocycle can be reconciled with its slow rate through a high activation energy; note the magnitude of the curve from the O level to the margin in Figure 6, top.

Part of the parallelly and perpendicularly polarized data are depicted in Figure 2 and Figures S.2 and S.3 of Supporting Information. Note the strong resemblance in shape with Figure 1, which points to small anisotropy differences, $r_{0,BR} - r_{0i}$. From the magnitude of the data, the estimated values of $r_{0,BR}$ of 0.29 for $H_2O$ and 0.40 for $D_2O$ (Table 2) are readily discernible. The estimated global anisotropy decay rate, $k_{tumb}$, reflecting membrane tumbling increased monotically from 0.008 to 0.046 $s^{-1}$ between 5 and 30 °C. At 35 °C, a smaller value of 0.020 $s^{-1}$ was estimated, which is very uncertain because at 35 °C the photocycle is practically complete after 10 ms. In general, the parallelly and perpendicularly polarized data were fitted less satisfactorily than the magic angle data (Figure 2 and Figures S.1−S.3 of Supporting Information). However, at 660 nm, the fit is very good, from which we conclude that the anisotropy differences for the K and O intermediate, $r_{0,BR} - r_{0,K}$ and $r_{0,BR} - r_{0,O}$, are close to zero in both $H_2O$ and $D_2O$. The 420 nm data for $H_2O$ and $D_2O$ agree in the estimate of $r_{0,BR} - r_{0,M_2}$. The early phase, until 100 $\mu$s, is estimated well in $H_2O$, and $r_{0,BR} - r_{0,M_1}$ is again close to zero. At later times, the fit gives rise to a relatively large $r_{0,BR} - r_{0,M_2}$ of 0.03. In $D_2O$, $M_1$ is formed much later and $M_1$ and $M_2$ cannot be well-resolved. Therefore, they were fitted with a common large $r_{0,BR} - r_{0i}$ (0.06). The $r_{0,BR} - r_{0,L}$ is estimated to be small, 0.01 and 0.02

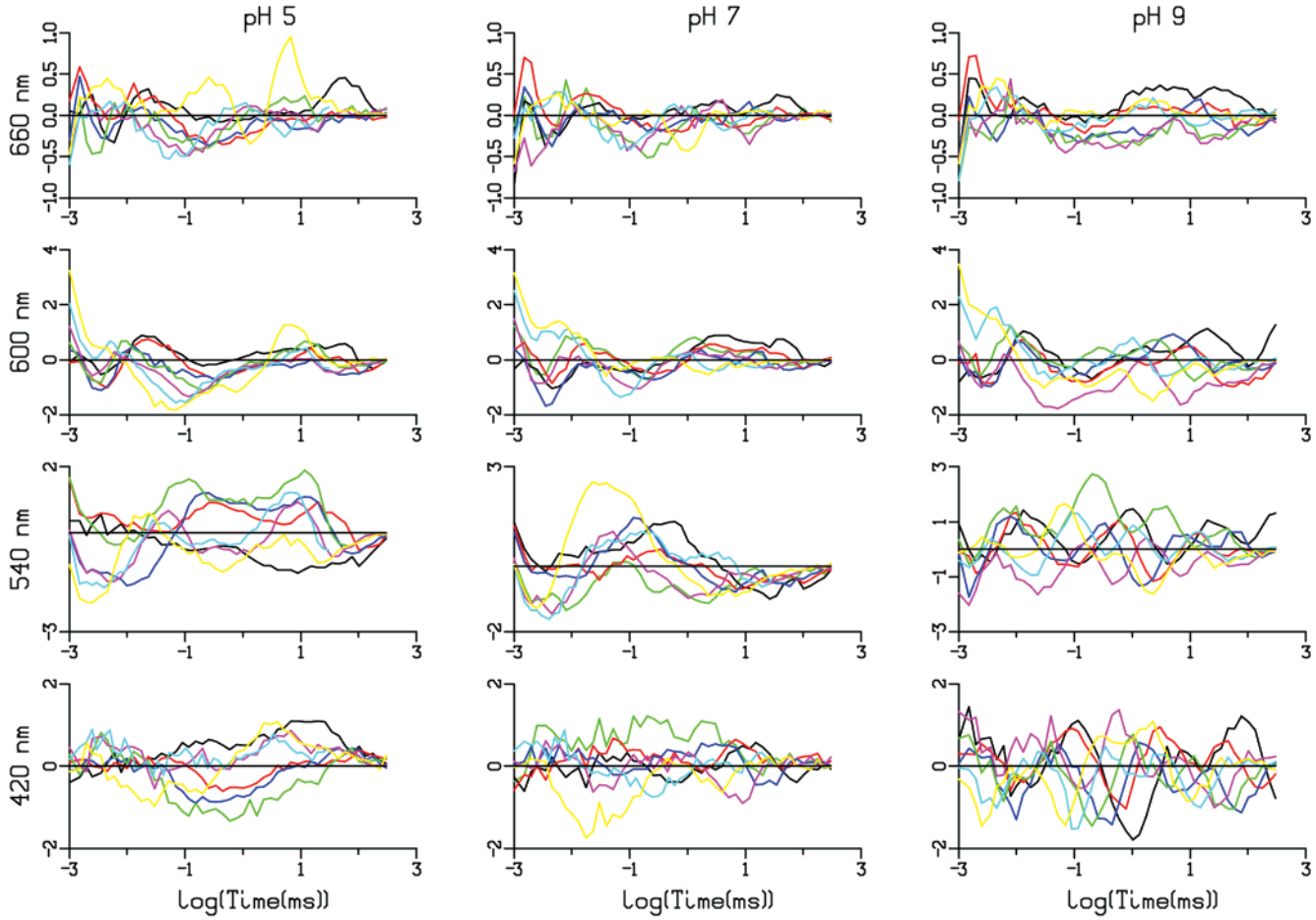


**Figure 3.** Residuals of the weighted fit of the (scaled) experimental magic angle data of Figure 1. From left to right, data are presented for pH 5, 7, and 9. At the left, each wavelength (420, 540, 600, or 660 nm) is written. The traces are shown at seven temperatures (5−35 °C in 5 °C steps; corresponding colors are black, red, blue, green, magenta, cyan, and yellow). Note the differences in vertical scale.

in $H_2O$ and $D_2O$, respectively. Both values are between the values for the K and $M_2$ intermediate. A discrepancy is present for $r_{0,BR} - r_{0,N}$; it is negligible in $H_2O$ and relatively large (0.06) in $D_2O$.

## Discussion

A good fit of the BR photocycle data at pH 5, pH 7, pH 9, and pD 7 and temperatures from 5 to 35 °C is possible with the reaction scheme K ⇌ L ⇌ $M_1$ ⇌ $M_2$ ⇌ N ⇌ O → BR. The major difference with the six intermediate scheme used in ref 15 is the modeling of the SAS using spectral assumptions (most importantly that the M states do not absorb above 540 nm) and a fraction cycling parameter. Note that, contrary to refs 20 and 26, here the spectrally silent transition from $M_1$ to $M_2$ is not irreversible and that the model is unbranched. The branchings in their analyses most probably result from the a priori choice of the SADS, as discussed earlier.[15] The resulting estimates for the free-energy levels appear reasonable. The SAS of Figure 5A are in accordance with the literature.[22,25,49] During the photocycle, the $M_2$ state shows a reduced anisotropy, indicating retinal reorientation. This supports the postulated mechanism that the $M_1$ to $M_2$ transition involves the switching of the hydrogen-bonding connection of the retinal Schiff base from the proton-release channel to the proton-uptake channel.[3−10,55] An ultimate test for the proposed model would be to use it with combined data from FTIR[53,54] and visible absorption difference spectroscopy. Borucki et al.[49] have elegantly shown that anisotropy data of oriented samples are also very informative.

There are several possible causes for the small trends in the residuals. (a) One is actinic flash intensity fluctuations. Allowing a refinement scaling parameter for each polarization condition (thereby tripling the number of scaling parameters) decreased the weighted rms error from 0.755 to 0.690. Furthermore, it is impossible to account for a small variation of the fraction cycling with wavelength. (b) Another is small temperature and pH/pD dependence of the spectra (both SAS and the ground-state spectrum). (c) A third is small temperature fluctuations. (d) A fourth is small systematic errors in the polarized measurements.[56,58] (e) The final possibility is an incomplete model. Attempts to fit the data with a model containing an additional, seventh, state ($L_2$, $M_3$, $N_2$, or P) did not result in an improved fit. Inclusion of pH-dependent branching[57] would be appropriate when analyzing measurements taken at more pH values.

**Comparisons.** Recently, Ludmann et al.[26] performed a similar study. Our methods and some of our results strikingly differ from theirs. Their analysis starts with the spectra estimated in ref 22 from which concentration profiles are estimated. Their kinetic scheme contains a $M_1$ ⇌ $M_2$ spectrally silent transition that becomes unidirectional above pH 6. Furthermore, their scheme contains a branch N → BR, the rate of which is larger than that of the N → O transition. Their raw data (except for 650 nm) show a trend of decreasing amplitude with increasing temperature, whereas we find an increase (compare Figure 1 with Figure 1 in ref 26). This may be due to the different preparations, they used membranes embedded in a gel and also an OD of about 1.4, whereas our membranes were in solution

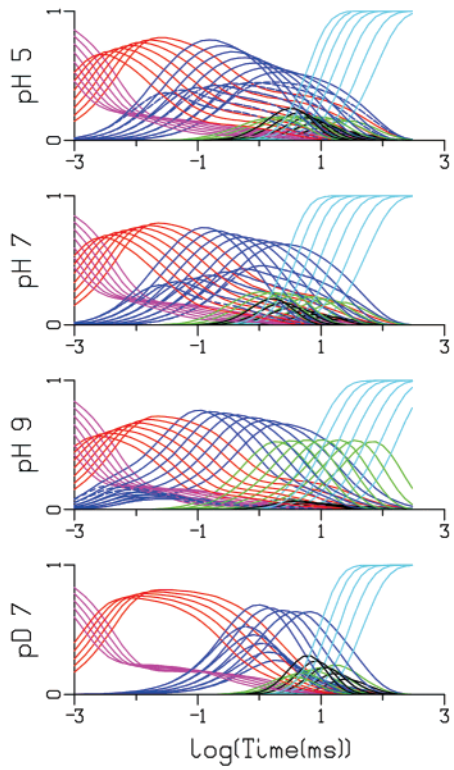


**Figure 4.** Time dependence of the (magic angle) species populations of the K ⇌ L ⇌ $M_1$ ⇌ $M_2$ ⇌ N ⇌ O → BR kinetic scheme from the target analysis. From top to bottom, data are presented for pH 5, 7, and 9 and pD 7. The concentration profiles are shown at seven temperatures (5−35 °C in 5 °C steps from right to left) or at five temperatures (10−30 °C in 5 °C steps from right to left) for pD 7. The species are denoted by colors as follows: magenta, K; red, L; blue, total M; green, N; black, O; cyan, BR. Dashed line indicates the $M_1$ population.

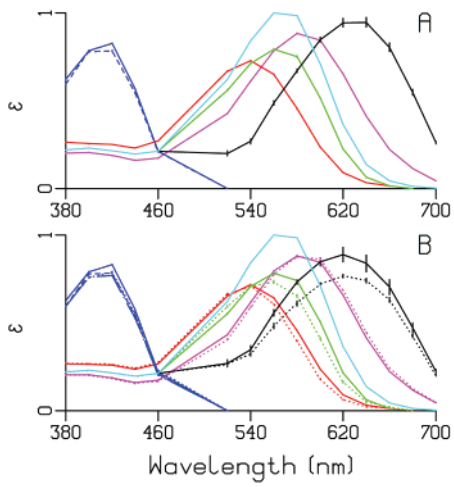


**Figure 5.** (A) SAS estimated from target analysis with K ⇌ L ⇌ $M_1$ ⇌ $M_2$ ⇌ N ⇌ O→BR kinetic scheme: magenta, K; red, L; blue, M; green, N; black, O; cyan, BR. Vertical bars indicate plus or minus estimated standard error. Dashed line indicates $M_1$ SAS, whereas solid line indicates $M_2$ SAS. Panel B shows the comparison of two sets of SAS estimated from $H_2O$ data using our model (solid lines) and the model from Ludmann et al.[26] (dotted). Further explanation is provided in the text.

with OD 0.3−0.5. Their backward rate $M_1$ → L is highest, and the $\Delta G$ level of $M_1$ is even higher than that of K. At pH 5 and pH 7, their $\Delta G$ level of $M_2$ is lower than that of N and O, and the backward rate N → $M_2$ is much higher. Judging from their $\Delta G$ level schemes, there is hardly any driving force for the photocycle, except for the transition from $M_1$ to $M_2$, which is unidirectional above pH 6. We find a more gradual decrease in $\Delta G$ going from K to O. After N, the results can no longer be compared because they used a branched model.

We fitted the $H_2O$ data with the model from ref 26 taking their estimated parameters as starting values. The fit converged to a different minimum, with a weighted rms error that was 10% larger, 0.832 (fit II) versus 0.753 (fit I). It is noticeable that during the fitting the rate of the branching reaction $k_{N\rightarrow BR}$ decreased about three times, whereas $k_{N\rightarrow O}$ increased by about the same amount. The very small starting values for $k_{M_2\rightarrow M_1}$ with pH 7 and pH 9 precluded convergence to the minimum found in fit I. The spectra estimated from these two fits of the $H_2O$ data are compared in Figure 5B. A number of small differences are discernible. The M, N, and O SAS estimated from fit I (solid lines) possess a larger amplitude than those from fit II (dotted lines). The L and N spectra of fit II show a small blue shift, whereas the K SAS shows a very small red shift. The small but distinct spectral differences found illustrate the fundamental drawback of the approach in which first spectra are derived on the basis of a number of assumptions, after which the resulting concentrations of the intermediates are fitted.

**Isotope Effect.** With pD 7, the L to M transition is strongly retarded (compare pH 7 in Figure 1 and pD 7 in Figure 2) in agreement with refs 37 and 38. This indicates strong involvement of proton translocation during this step. The increase in the $\Delta G$ level of the L ⇌ $M_1$ transition state appears to be due to a decrease of $\Delta S^{\#}$ of the L → $M_1$ transition (green curve in bottom panel of Figure 6). This supports the hypothesis of LeCoutre and Gerwert,[37] who explain the anomalous isotope effect by an ice-like mechanism, in which the proton is expelled from a highly ordered protein environment into the less-ordered aqueous bulk phase. Alternatively, the large kinetic isotope effect points to the necessity of including proton-tunneling corrections to classical transition-state theory.[59]

**Anisotropy.** Several groups[60−64] have reported anomalous behavior of the anisotropy on a millisecond time scale. Groma et al.[65] observed unusual time-dependent anisotropy with immobilized BR, also. With pH 7 and pH 9 for wavelengths between 520 and 640 nm, a sign reversal of the time-resolved linear dichroism (and thus of $r(t,\lambda)$) was observed by us, too (see Figure S.4 of Supporting Information) but not with pH 5 or pD 7. This late anisotropy sign reversal, if it is not an artifact, cannot be explained by the simple model of eq 6. Several alternative explanations have been put forward,[60−65] but prerequisites for testing them are a well-established model for the magic angle data and more informative data in the relevant time range across wavelength and temperature, preferably with immobilized BR. Recently, Borucki et al.[49] elegantly resolved the anisotropy changes of K, L, and M in oriented purple membranes. The largest anisotropy change they found in L, which is at variance with our results in solution. We cannot exclude polarization artifacts as described in ref 56. The very small anisotropy change in K and the larger change in $M_2$ agree with their results. The contradictions in the literature are elaborately discussed in refs 49 and 66. With pD 7, the anisotropy of BR was 0.4, as expected (Table 2). The far from perfect anisotropy of 0.29 in $H_2O$ is attributed to polarization artifacts.[56]

**Target Analysis.** The spectrotemporal model used here is much more simple and flexible than the skewed Gaussian function used before to describe spectra.[32,34,35] When the number of wavelengths is relatively small, it becomes advantageous to

**TABLE 1: Thermodynamic Parameters, $k_{20}$ ($s^{-1}$) and $\Delta H^{\#}$ (kJ/mol) Estimated from Target Analysis of BR Photocycle Data from 5 to 35 °C**

| | pH 5 | | pH 7 | | pH 9 | | pD 7 | |
|---|---|---|---|---|---|---|---|---|
| transition | $k_{20}$ | $\Delta H^{\#}$ | $k_{20}$ | $\Delta H^{\#}$ | $k_{20}$ | $\Delta H^{\#}$ | $k_{20}$ | $\Delta H^{\#}$ |
| K → L | 412 000 ± 2000 | 40 ± 1 | 428 000 ± 2000 | 40 ± 1 | 454 000 ± 3000 | 40 ± 1 | 338 000 ± 3000 | 36 ± 1 |
| L → $M_1$ | 11 200 ± 400 | 77 ± 1 | 11 400 ± 700 | 74 ± 6 | 168 000 ± 15000 | 29 ± 10 | 1480 ± 20 | 66 ± 1 |
| $M_1$ → $M_2$ | 2400 ± 1200 | 119 ± 20 | 3800 ± 1200 | 100[a] | 46 100 ± 700 | 46 ± 2 | 650 ± 80 | 9[a] |
| $M_2$ → N | 440 ± 100 | 24 ± 2 | 490 ± 70 | 52[a] | 227 ± 5 | 83 ± 1 | 300 ± 30 | 74 ± 7 |
| N → O | 370 ± 50 | 69 ± 2 | 500 ± 70 | 68 ± 20 | 64 ± 20 | 71 ± 5 | 310 ± 70 | 85 ± 10 |
| O → BR | 330 ± 60 | 21 ± 1 | 700 ± 120 | 31 ± 2 | 570 ± 90 | 37 ± 3 | 200 ± 40 | 23 ± 1 |
| K ← L | 107 000 ± 1000 | 51 ± 1 | 110 000 ± 1000 | 48 ± 1 | 122 000 ± 1300 | 48 ± 3 | 88 500 ± 1000 | 48 ± 1 |
| L ← $M_1$ | 6800 ± 700 | 65 ± 7 | 6700 ± 1000 | 69[a] | 765 000 ± 80 000 | 0[a] | 645 ± 40 | 36 ± 7 |
| $M_1$ ← $M_2$ | 3300 ± 1300 | 74 ± 30 | 2600 ± 500 | 78[a] | 2290 ± 120 | 53 ± 3 | 160 ± 100 | 60 ± 30 |
| $M_2$ ← N | 78 ± 7 | 36[a] | 120 ± 20 | 17[a] | 44 ± 1 | 107 ± 2 | 250 ± 140 | 55 ± 20 |
| N ← O | 210 ± 70 | 54 ± 7 | 470 ± 100 | 51 ± 40 | 345 ± 150 | 31 ± 15 | 73 ± 20 | 48 ± 25 |

[a] Parameter cannot be reliably estimated.

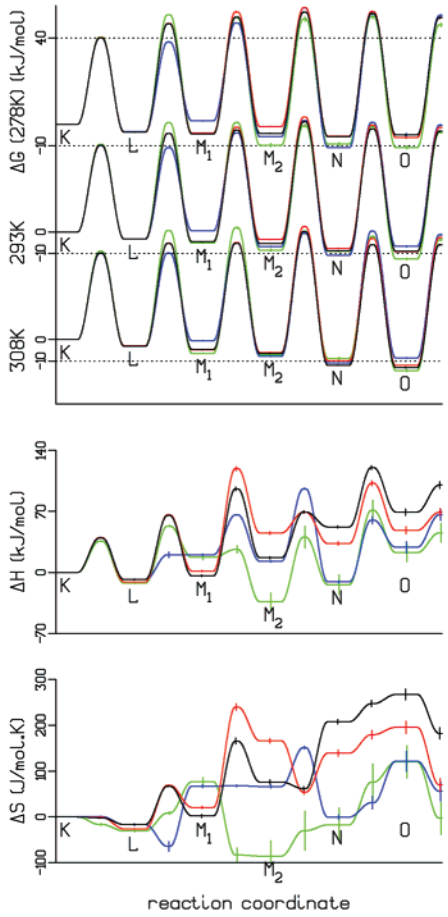


**Figure 6.** Free energy (top), enthalpy (middle), and entropy changes (bottom) relative to K during the photocycle estimated from target analysis. The $\Delta G$ minima correspond, from left to right, to K, L, $M_1$, $M_2$, N, and O, whereas the maxima correspond to the transition states. The horizontal dotted lines at 40 and −10 kJ/mol coincide for diagrams corresponding to the successive temperatures. The colors indicate the following: black pH 5; red pH 7; blue pH 9; green pD 7. Vertical bars indicate plus or minus standard error.

use spectral assumptions in combination with (conditionally linear) free amplitude parameters, instead of a functional description of spectra requiring a handful of (nonlinear) parameters. The direct estimation of all SAS provides an important test criterion.

We spend great effort to minimize the number of parameters, but we still need 193 thermodynamic, spectral, anisotropy, and scaling parameters, disregarding the 235 scaling parameters, which are estimated during refinement. The parameters describing the $M_1 \rightleftharpoons M_2$ transition are particularly hard to estimate (Table 1).

**TABLE 2: Summary of Estimated Anistropy Parameters, $r_{0,BR} - r_{0i}$ and $r_{0,BR}$[a]**

| state | $H_2O$ | $D_2O$ |
|---|---|---|
| K | 0.005 | 0 |
| L | 0.01 | 0.02 |
| $M_1$ | 0 | |
| $M_2$ | 0.03 | 0.06 |
| N | 0 | 0.06 |
| O | 0 | 0.006 |
| BR | 0.29 | 0.40 |

[a] Estimated error is 1 in the last digit.

The strength of the target analysis using the spectrotemporal model is that by using spectral constraints (and by imposing nonnegative activation enthalpies) the unrealistic physicochemical parameters estimated in ref 15 have been avoided. Thus basically, the parameter search space has been made smaller (less parameters, some constrained parameters).

Ideally, a spectrotemporal measurement, using, for example, a streak camera,[67] which in combination with a polychromator monitors spectral changes during a sweep, would provide a way to circumvent the errors caused by laser intensity fluctuations. The fc target analysis has also been successfully applied (results not shown) to the photocycle of photoactive yellow protein, which contains the blue-shifted intermediate pB.[32] It would be interesting to try it with sensory rhodopsin II.[68]

Our target analysis bears on two fundamental issues regarding the nature of the "protonation switch" responsible for vectorial transport.[69] Is the switch unidirectional? According to Ludmann et al.,[26] the M1 ⇌ M2 spectrally silent transition becomes unidirectional above pH 6. In contrast, we have shown that an equilibrium at all pH's provides, in fact, a better description of the data. Furthermore, in view of the gradual change of the free energy, the switch does not appear to be a single step but rather is the directional aspect of all photocycle reactions. The recovery step, O → BR, where, according to our model, most free energy (about 20 kJ/mol) is dissipated, ensures the unidirectionality of transport. According to Lanyi,[5] this free energy dissipation ensures that proton back-pressure does not cause accumulation of intermediate states.

In conclusion, to our knowledge, this is the first simultaneous analysis of a five-dimensional data set. Ludmann et al.[26] dissected their four-dimensional data set by fitting with the spectra estimated in ref 22 after which the estimated concentrations of the intermediates were fitted. Borucki et al.[49] also needed the assumption that the M state does not absorb above

520 nm to estimate the fraction cycling. They analyzed their time-resolved spectra at each condition of pH and temperature, separately. It would be of interest to analyze these other data sets using the fc target analysis proposed here.

**Acknowledgment.** We are indebted to Aihua Xie for her collaboration in the experiments. We thank Aihua Xie, Rienk van Grondelle, Thomas Gensch, Klaas Hellingwerf, Wouter Hoff, Frank van Mourik, and John Nagle for critically reading the manuscript and helpful discussions.

**Supporting Information Available:** Figures S1−S4 presenting the residuals of Figure 2, fits of the parallel and perpendicular polarization data of the BR photocycle at pH 5, 7, and 9, and fits of time-resolved linear dichroism data of the BR photocycle at pH 5, 7, and 9 and pD 7. This material is available free of charge via the Internet at http://pubs.acs.org.

## References and Notes

(1) Ebrey, T. G. In *Thermodynamics of Membrane Receptors and Channels*; Jackson, M. B., Ed.; CRC: Boca Raton, FL, 1993; Chapter 10.
(2) Haupts, U.; Tittor, J.; Oesterhelt, D. *Annu. Rev. Biophys. Biomol. Struct.* **1999**, *28*, 367−399.
(3) Heberle, J. *Biochim. Biophys. Acta* **2000**, *1458*, 135−147.
(4) Lanyi, J. K. *Biochim. Biophys. Acta* **1993**, *1183*, 241−261.
(5) Lanyi, J. K. *FEBS Lett.* **1999**, *464*, 103−107.
(6) Lanyi, J. K. *J. Phys. Chem. B* **2000**, *104*, 11441−11448.
(7) Luecke, H.; Schobert, B.; Richter, H.-T.; Cartailler, J. P.; Lanyi, J. K. *J. Mol. Biol.* **1999**, *291*, 899−911.
(8) Luecke, H.; Schobert, B.; Richter, H.-T.; Cartailler, J. P.; Lanyi, J. K. *Science* **1999**, *286*, 255−260.
(9) Mathies, R. A.; Lin, S. W.; Ames, J. B.; Pollard, W. T. *Annu. Rev. Biophys. Biophys. Chem.* **1991**, *20*, 491−518.
(10) Oesterhelt, D. *Curr. Opin. Struct. Biol.* **1998**, *8*, 489−500.
(11) Lozier, R. H.; Bogomolni, R. A.; Stoeckenius, W. *Biophys. J.* **1975**, *15*, 955−962.
(12) Ames, J. B.; Mathies, R. A. *Biochemistry* **1990**, *29*, 7181−7190.
(13) Hessling, B.; Souvignier, G.; Gerwert, K. *Biophys. J.* **1993**, *65*, 1929−1941.
(14) Lanyi, J. K.; Váró, G. *Isr. J. Chem.* **1995**, *35*, 365−385.
(15) Lozier, R. H.; Xie, A.; Hofrichter, J.; Clore, G. M. *Proc. Natl. Acad. Sci. U.S.A.* **1992**, *89*, 3610−3614.
(16) Chizhov, I.; Chernavskii, D. S.; Engelhard, M.; Mueller, K.-H.; Zubov, B. V.; Hess, B. *Biophys. J.* **1996**, *71*, 2329−2345.
(17) Xie, A. H.; Nagle, J. F.; Lozier, R. H. *Biophys. J.* **1987**, *51*, 627−635.
(18) Nagle, J. F. *Photochem. Photobiol.* **1991**, *54*, 897−903.
(19) Betancourt, F. M. H.; Glaeser, R. M. *Biochim. Biophys. Acta* **2000**, *1460*, 106−118.
(20) Váró, G.; Lanyi, J. K. *Biochemistry* **1991**, *30*, 5008−5015.
(21) Váró, G.; Lanyi, J. K. *Biochemistry* **1991**, *30*, 5016−5022.
(22) Gergely, C.; Zimányi, L.; Váró, G. *J. Phys. Chem. B.* **1997**, *101*, 9390−9395.
(23) Zimányi, L.; Kulcsár, A.; Lanyi, J. K.; Sears, D. F.; Saltiel, J. *Proc. Natl. Acad. Sci. U.S.A.* **1999**, *96*, 4408−4413.
(24) Zimányi, L.; Kulcsár, A.; Lanyi, J. K.; Sears, D. F.; Saltiel, J. *Proc. Natl. Acad. Sci. U.S.A.* **1999**, *96*, 4414−4419.
(25) Kulcsár, A.; Saltiel, J.; Zimányi, L. *J. Am. Chem. Soc.* **2001**, *123*, 3332−3340.
(26) Ludmann, K.; Gergely, C.; Váró, G. *Biophys. J.* **1998**, *75*, 3110−3119.
(27) Dér, A.; Oroszi, L.; Kulcsár, A.; Zimányi, L.; Toth-Boconádi, R.; Keszthelyi, L.; Stoeckenius, W.; Ormos, P. *Proc. Natl. Acad. Sci. U.S.A.* **1999**, *96*, 2776−2781.
(28) Hendler, R. W.; Shrager, R. I.; Bose, S. *J. Phys. Chem. B.* **2001**, *105*, 3319−3328.
(29) Nagle, J. F. *Biophys. J.* **1991**, *59*, 476−487.
(30) Beechem, J. M.; Ameloot, M.; Brand, L. *Anal. Instrum.* **1985**, *14*, 379−402.
(31) Holzwarth, A. R. In *Biophysical Techniques in Photosynthesis*; Amesz, J., Hoff, A. J., Eds.; Kluwer: Dordrecht, The Netherlands, 1996; Chapter 5.
(32) Hoff, W. D.; van Stokkum, I. H. M.; van Ramesdonk, H. J.; van Brederode, M. E.; Brouwer, A. M.; Fitch, J. C.; Meyer, T. E.; van Grondelle, R.; Hellingwerf, K. J. *Biophys. J.* **1994**, *67*, 1691−1705.
(33) Krueger, B. P.; Lampoura, S. S.; van Stokkum, I. H. M.; Papagiannakis, E.; Salverda, J. M.; Gradinaru, C. C.; Rutkauskas, D.; Hiller, R. G.; van Grondelle, R. *Biophys. J.* **2001**, *80*, 2843−2855.
(34) Van Stokkum, I. H. M.; Scherer, T.; Brouwer, A. M.; Verhoeven, J. W. *J. Phys. Chem.* **1994**, *98*, 852−866.
(35) Van Stokkum, I. H. M. *IEEE Trans. Instrum. Meas.* **1997**, *46*, 764−768.
(36) Dioumaev, A. K. *Biophys. Chem.* **1997**, *67*, 1−25.
(37) Le Coutre, J.; Gerwert, K. *FEBS Lett.* **1996**, *398*, 333−336.
(38) Brown, L. S.; Needleman, R.; Lanyi, J. K. *Biochemistry* **2000**, *39*, 938−945.
(39) Lozier, R. H. *Methods Enzymol.* **1982**, *88*, 133−162.
(40) Seber, G. A. F.; Wild, C. J. *Nonlinear regression*; Wiley: New York, 1989.
(41) Golub, G. H.; LeVeque, R. J. *Proc. 1979 Army Numer. Anal. Comput. Conf.; ARO Rep.* **1979**, *79-3*, 1−12.
(42) Laidler, K. J. *Chemical kinetics*, 3rd ed.; Harper & Row: New York, 1987.
(43) Nagle, J. F.; Zimanyi, L.; Lanyi, J. K. *Biophys. J.* **1995**, *68*, 1490−1499.
(44) Müller, K. H.; Plesser, T. *Eur. Biophys. J.* **1991**, *19*, 231−240.
(45) Althaus T.; Stockburger, M. *Biochemistry* **1998**, *37*, 2807−2817.
(46) Balashov, S. P.; Govindjee, R.; Ebrey, T. G. *Biophys. J.* **1991**, *60*, 475−490.
(47) Hanomoto, J. H.; Dupuis, P.; El-Sayed, M. A. *Proc. Natl. Acad. Sci. U.S.A.* **1984**, *81*, 7083−7088.
(48) Váró, G.; Lanyi, J. K. *Biochemistry* **1990**, *29*, 2241−2250.
(49) Borucki, B.; Otto, H.; Heyn, M. P. *J. Phys. Chem. B.* **1999**, *103*, 6371−6383.
(50) Balashov, S. P.; Lu, M.; Imasheva, E. S.; Govindjee, R.; Ebrey, T. G.; Othersen, B.; Chen, Y. M.; Crouch, R. K.; Menick, D. R. *Biochemistry* **1999**, *38*, 2026−2039.
(51) Logunov, S. L.; El-Sayed, M. A. *J. Phys. Chem. B.* **1997**, *101*, 6629−6633.
(52) Zhang, D.; Mauzerall, D. *Biophys. J.* **1996**, *71*, 381−388.
(53) Rodig, C.; Chizhov, I.; Weidlich, O.; Siebert, F. *Biophys. J.* **1999**, *76*, 2687−2701.
(54) Zscherp, C.; Schlesinger, R.; Tittor, J.; Oesterhelt, D.; Heberle, J. *Proc. Natl. Acad. Sci. U.S.A.* **1999**, *96*, 5498−5503.
(55) Subramaniam, S.; Lindahl, I.; Bullough, P.; Faruqi, A. R.; Tittor, J.; Oesterhelt, D.; Brown, L.; Lanyi, J.; Henderson, R. *J. Mol. Biol.* **1999**, *287*, 145−161.
(56) Lewis, J. W.; Kliger, D. S. *Photochem. Photobiol.* **1991**, *54*, 963−968.
(57) Balashov, S. P. *Biochim. Biophys. Acta* **2000**, *1460*, 75−94.
(58) Nagle, J. F.; Bhattacharjee, S. M.; Parodi, L. A.; Lozier, R. H. *Photochem. Photobiol.* **1983**, *38*, 331−339.
(59) Scheiner, S. *Biochim. Biophys. Acta* **2000**, *1458*, 28−42.
(60) Wan, C.; Qian, J.; Johnson, C. K. *Biophys. J.* **1993**, *65*, 927−938.
(61) Song, Q.; Harms, G. S.; Wan, C.; Johnson, C. K. *Biochemistry* **1994**, *33*, 14026−14033.
(62) Harms, G. S.; Song, Q.; Johnson, C. K. *Biophys. J.* **1996**, *70*, 2352−2357.
(63) Harms, G. S.; Johnson, C. K. *Photochem. Photobiol.* **1997**, *66*, 133−139.
(64) Kikukawa, T.; Araiso, T.; Shimozawa, T.; Mukasa, K.; Kamo, N. *Biophys. J.* **1997**, *73*, 357−366.
(65) Groma, G. I.; Bogomolni, R. A.; Stoeckenius, W. *Biochim. Biophys. Acta* **1997**, *1319*, 69−85.
(66) Heyn, M. P.; Borucki, B.; Otto, H. *Biochim. Biophys. Acta* **2000**, *1460*, 60−74.
(67) Ito, T.; Hiramatsu, M.; Hosoda, M.; Tsuchiya, Y. *Rev. Sci. Instrum.* **1991**, *62*, 1415−1419.
(68) Chizhov, I.; Schmies, G.; Seidel, R.; Sydor, J. R.; Luttenberg, B.; Engelhard, M. *Biophys. J.* **1998**, *75*, 999−1009.
(69) Lanyi, J. K. *Biochim. Biophys. Acta* **2000**, *1460*, 1−3.

Ivo H.M. van Stokkum and Richard H. Lozier
Target analysis of the bacteriorhodopsin photocycle using a spectrotemporal model

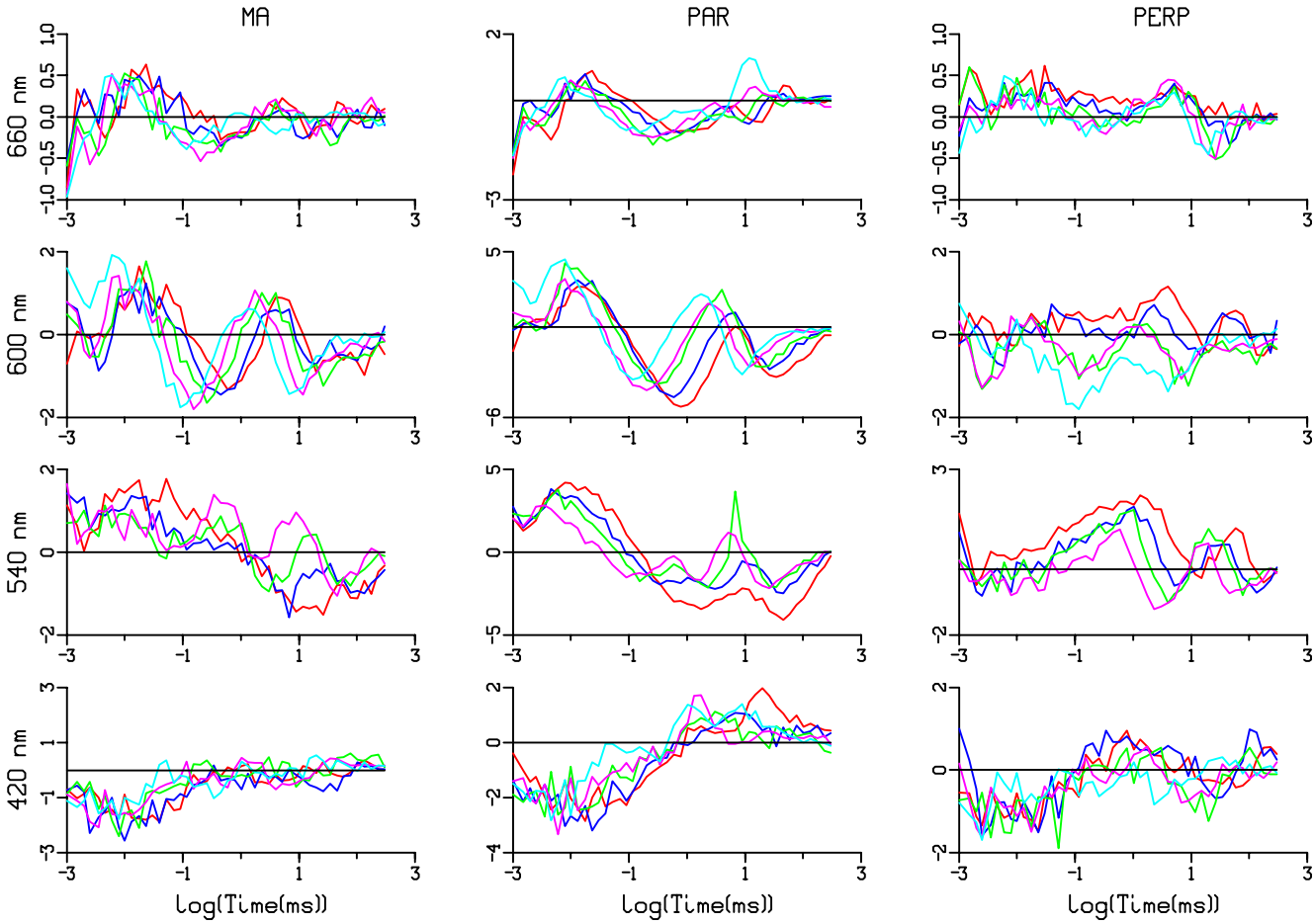


Fig. S.1. Residuals of the weighted fit of the (scaled) pD 7 experimental data of Fig. 2. From left to right: magic angle, parallel, and perpendicular polarization. At the left each wavelength (420, 540, 600 or 660 nm) is written. The traces are shown at five temperatures (10–30 ˚C in 5 ˚C steps, corresponding colors are red, blue, green, magenta, cyan). Note the differences in vertical scale.

Ivo H.M. van Stokkum and Richard H. Lozier
Target analysis of the bacteriorhodopsin photocycle using a spectrotemporal model

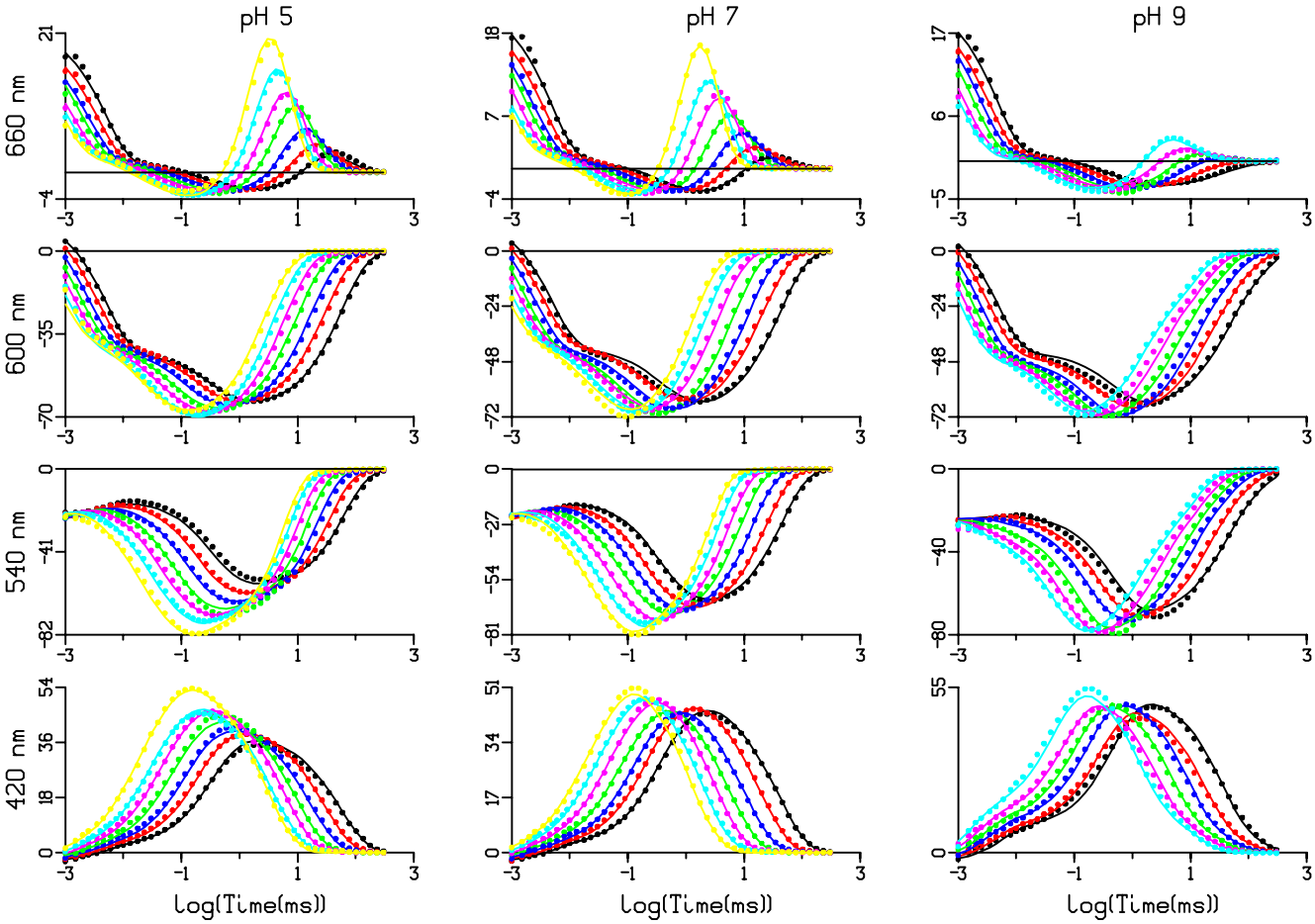


Fig. S.2. Comparison of the (scaled) parallel polarization data of the BR photocycle (dots) and fit curves obtained using the spectrotemporal model with kinetic scheme $K \rightleftharpoons L \rightleftharpoons M_1 \rightleftharpoons M_2 \rightleftharpoons N \rightleftharpoons O \rightarrow BR$. From left to right: pH 5, pH 7, pH 9. At the left each wavelength (420, 540, 600 or 660 nm) is written. The traces are shown at seven temperatures (5–35 ˚C in 5 ˚C steps from right to left, corresponding colors are black, red, blue, green, magenta, cyan, yellow). Note the differences in vertical scale.

Ivo H.M. van Stokkum and Richard H. Lozier
Target analysis of the bacteriorhodopsin photocycle using a spectrotemporal model

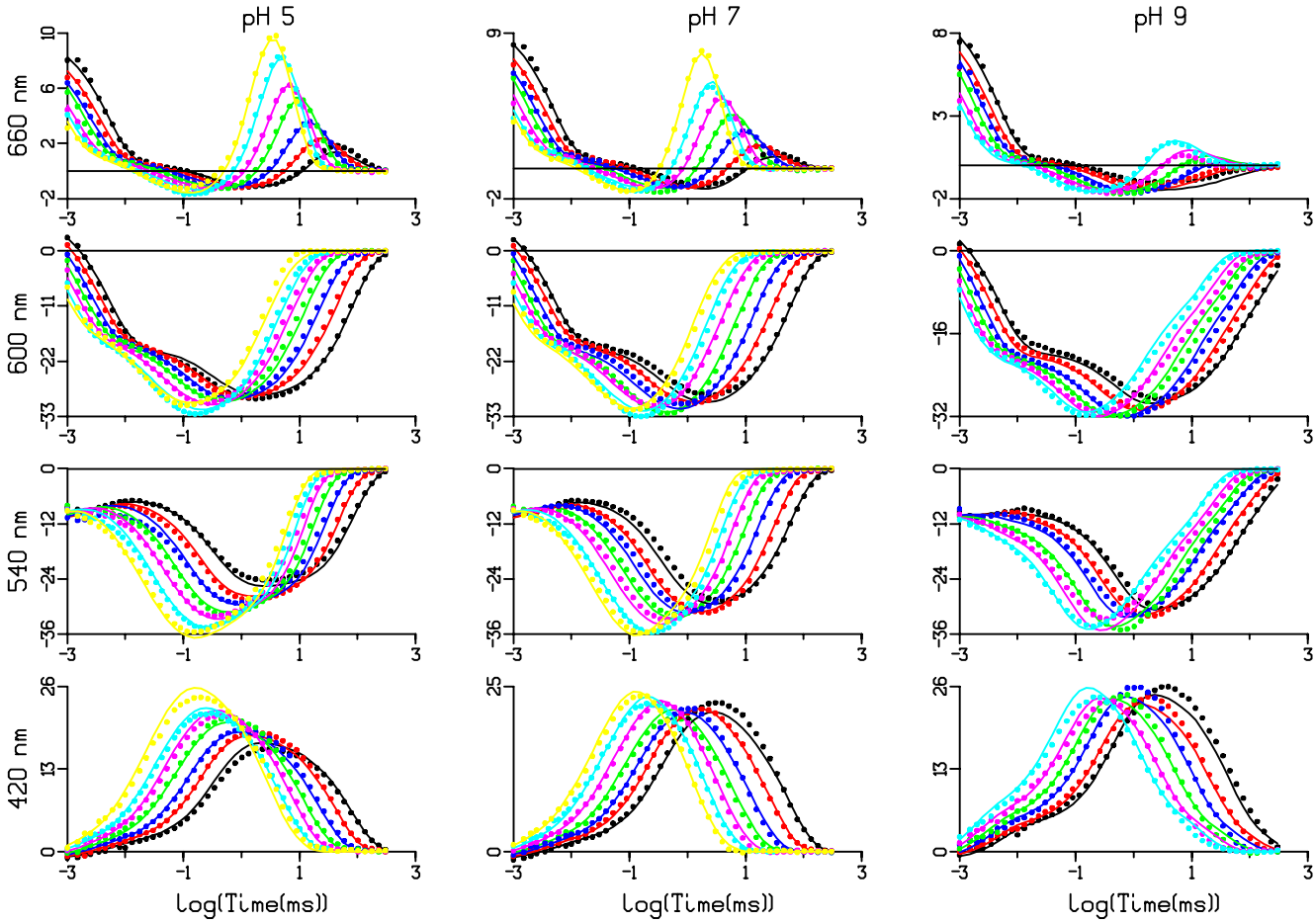


Fig. S.3. Comparison of the (scaled) perpendicular polarization data of the BR photocycle (dots) and fit curves obtained using the spectrotemporal model with kinetic scheme K $\rightleftharpoons$ L $\rightleftharpoons$ $M_1$ $\rightleftharpoons$ $M_2$ $\rightleftharpoons$ N $\rightleftharpoons$ O $\rightarrow$ BR. From left to right: pH 5, pH 7, pH 9. At the left each wavelength (420, 540, 600 or 660 nm) is written. The traces are shown at seven temperatures (5–35 ˚C in 5 ˚C steps from right to left, corresponding colors are black, red, blue, green, magenta, cyan, yellow). Note the differences in vertical scale.

Ivo H.M. van Stokkum and Richard H. Lozier
Target analysis of the bacteriorhodopsin photocycle using a spectrotemporal model

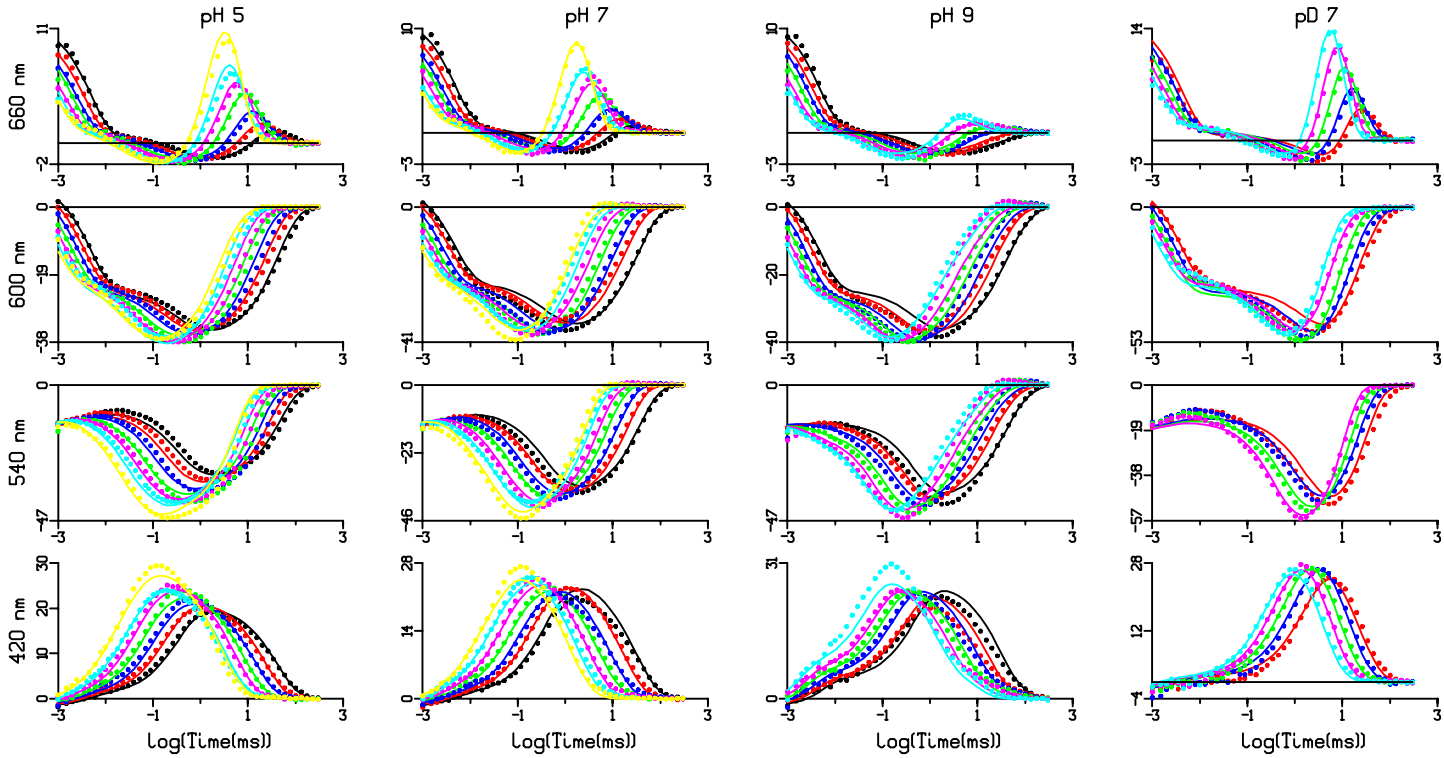


Fig. S.4. Time resolved linear dichroism data of the BR photocycle (dots) and fit curves obtained using the spectrotemporal model with kinetic scheme K $\rightleftharpoons$ L $\rightleftharpoons$ $M_1$ $\rightleftharpoons$ $M_2$ $\rightleftharpoons$ N $\rightleftharpoons$ O $\rightarrow$ BR. From left to right: pH 5, pH 7, pH 9, pD 7. At the left each wavelength (420, 540, 600 or 660 nm) is written. The traces are shown at seven temperatures (5–35 ˚C in 5 ˚C steps from right to left, corresponding colors are black, red, blue, green, magenta, cyan, yellow). Note the differences in vertical scale.

Note the sign reversal with pH 7 and pH 9 for wavelengths of 540 and 600 nm, but not with pH 5 or pD 7.